BACHELOR THESIS

In-situ Transmission Electron Microscopy and Density Functional Theory Study of the Reduction of MoO_3 Nanoparticles

Author:
Roos de Boer

Supervisors:
Dr. Marijn van Huis
MSc. Xiaodan Chen

June 11, 2020

Soft Condensed Matter & Biophysics
Debye Institute for Nanomaterials Science

Utrecht University

Abstract

Molybdenum trioxide (MoO_3) nanoparticles were heated using in-situ transmission electron microscopy (TEM), causing the nanoparticles to disintegrate into smaller flakes. These nanoparticle flakes were shown to be MoO_2 and Mo_4O_{11}. The MoO_3 nanoparticle also exfoliated partly before reducing. The findings from the heating were investigated with density functional theory (DFT) calculations using the Vienna ab initio simulation package (VASP). It was found that the reduction to neither MoO_2 nor Mo_4O_{11} is favourable at 0 K, but the temperature raise and the vacuum of the TEM probably shift the equilibrium so that the reduction takes place. It was found that the formation of Mo_4O_{11} probably happens in a side reaction, such that the MoO_3 reduction to MoO_2 is a one-step reaction. The exfoliation energy was calculated and the disintegration of the nanoparticle was concluded to be caused by the large lattice mismatch of the MoO_3/MoO_2 interface.

Key words: Molybdenum oxides, in-situ transmission electron microscopy, density functional theory, reduction, nanoparticles, VASP

Contents

1. Introduction

Molybdenum trioxide (MoO_3) is the molybdenum oxide with the highest oxidation state. An interesting property of molybdenum oxide is the vast amount of different substoichiometric phases it has. These Magnéli oxides have an oxidation number ranging from 3 to 2, and result from oxygen defects that lead to the formation of a new crystallographic structure [1]. MoO_3 can be fabricated at the nano scale [2, 3], which acts as a great compound for selective oxidation catalysis [4, 5].

There are two reduction mechanisms believed to apply for the reduction of MoO_3 to MoO_2. The first is a one-step reaction, in which orthorhombic MoO_3 immediately reduces to monoclinic MoO_2. The second is a two-step reduction, first suggested by Burch [6], in which Mo_4O_{11} is an intermediate product. Ressler et al. [7] reported that the MoO_3 reduction with hydrogen is a one-step process without crystalline intermediates below 698 K, but at temperatures above 698 K, Mo_4O_{11} was formed. They reported, however, that Mo_4O_{11} is not an intermediate, but is formed during a parallel reaction. Spevack and McIntyre [8] reported to have found several intermediates in their thermal reduction of MoO_3 to MoO_2, and that the presence of impurities affects the reduction causing the intermediates to form.

Orthorhombic MoO_3 has a layered structure with van der Waals interactions between the layers. Monoclinic MoO_2 has a deformed rutile structure. Both MoO_3 and MoO_2 are composed of MoO_6 octahedra. Mo_4O_{11} however, which is most found in the orthorhombic form, is composed of MoO_4 tetrahedra, like in a ReO_3 structure. Figure 1 shows the molybdenum oxide crystal structures.

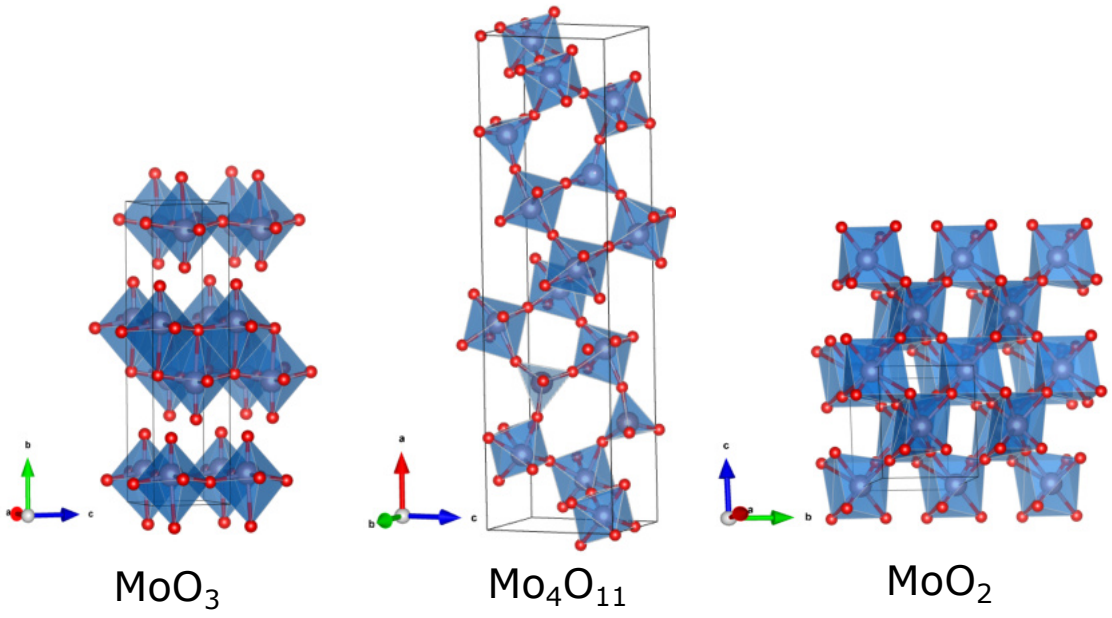

Figure 1: Crystal structures of different molybdenum oxides.

In this thesis, the reduction mechanism of orthorhombic MoO_3 nanoparticles is investigated with in-situ transmission electron microscopy. Mainly the potential appearance of Mo_4O_{11} is of interest. In addition, density functional theory (DFT) is used to investigate the energetics of the MoO_3 nanoparticles reduction. DFT is a quantummechanical computational method that uses the Schrödinger equation to perform calculations on molecules and crystal structures. Using DFT, the stability of the different molybdenum oxide phases will be assessed and the reaction energies calculated.

2. Theory

2.1. Transmission electron microscopy

Transmission electron microscopy (TEM) has become one of the most used characterization instrument in materials science. A TEM can be seen as an optical microscope with the ability to measure diffraction. Since a TEM uses electrons to form images, a much higher resolution can be obtained compared to an optical microscope. To study the reduction of MoO_3, in-situ TEM is used, which enables the heating of the sample while it is in the microscope. All TEM measurements for this thesis were performed on a FEI Talos F200X TEM.

An overview image of a typical TEM can be seen in figure 2. Apart from the conventional imaging, a TEM often has the ability to perform scanning transmission electron microscopy (STEM) and is equipped with different spectroscopic techniques among which energy-dispersive x-ray spectroscopy (EDS) and electron energy-loss spectroscopy (EELS). These techniques will not be discussed in this thesis.

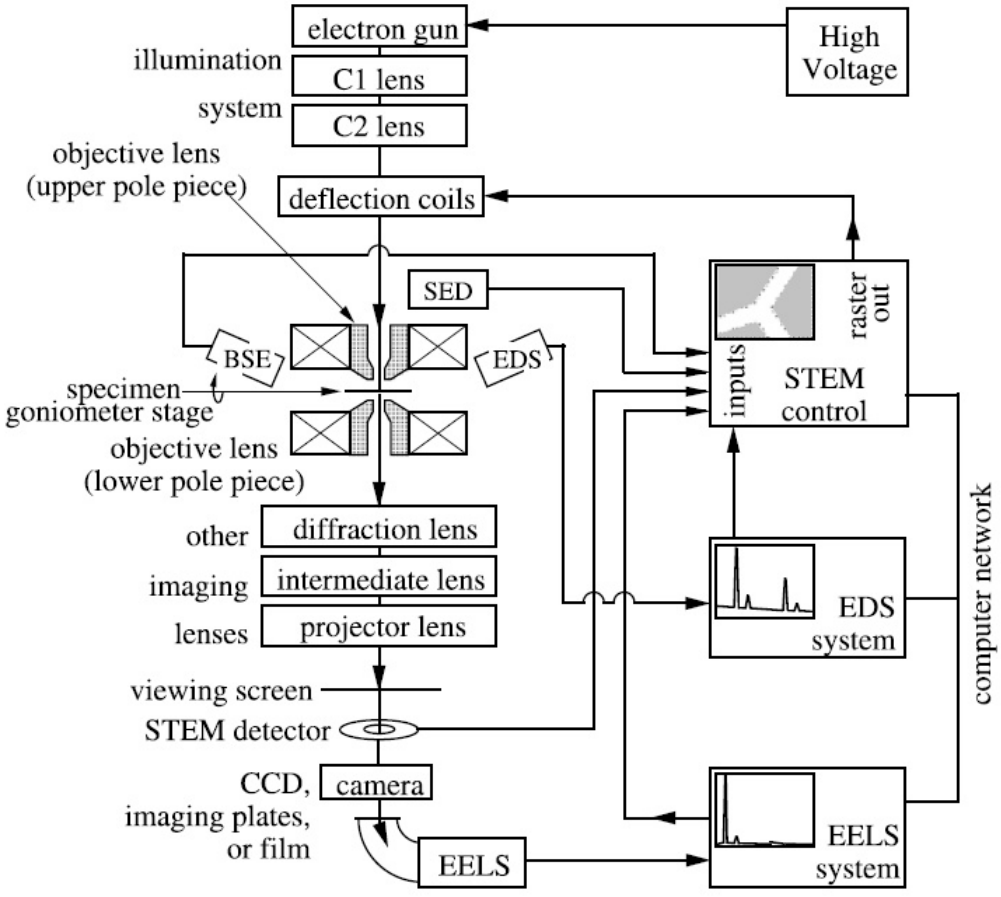

Figure 2: Overview of a typical TEM system. Reprinted from [9].

Images are created in the TEM by transmitting a beam of electrons through a thin sample. The electron source of the TEM is located in the upper part of the microscope and consists of a cathode and anode. Electrons are emitted from an electron gun, of which there are two types. A thermionic gun uses heat to emit electrons from a metal. Formerly, a tungsten wire was used as the metal. However, high temperatures had to be reached to overcome the workfunction of the tungsten/vacuum interface which led to evaporation of the tungsten wire and therefore a short lifetime. Later, LaB_6 was used as the metal because of its lower workfunction, which improved the lifetime of the electron gun by approximately a factor of 10. The second type of electron gun is a field emission gun (FEG), which is used in most high-end TEMs nowadays, including the FEI Talos F200X. In an FEG, a positive electrode is placed near a pointed metal tip which is usually made of tungsten. The potential gradient causes electrons to overcome the workfunction. An FEG has a longer lifetime than a thermionic gun. A FEG also has a more coherent electron beam because of the lower thermal energy spread.

After the electrons are emitted, they are focused into a beam and accelerated by the positive potential of the anode. Several electromagnetic lenses focus the electron beam and apertures are used to restrict the beam. The specimen holder is attached to a mechanical arm, which is controlled by a computer and allows for small and precise rotations and translations.

The images are created using the fact that the amount of transmitted and diffracted electrons is different for different materials and thicknesses. There are two modes for imaging, bright-field and dark-field. If all transmitted and diffracted rays are used to form an image, the sample will show less contrast. In order to improve the contrast, an objective aperture is used to block parts of the rays. In bright-field (BF) mode, the objective aperture passes the direct beam. The areas with lower electron transmittance will form dark spots, and the areas with high electron transmittance form bright spots on the image. In dark-field (DF) mode, the objective aperture blocks the direct beam, but allows a diffracted beam to pass. This results in bright areas where electron diffraction is high, and dark areas where electron diffraction is low.

High-resolution TEM (HRTEM) enables imaging with atomic resolution. The conventional bright-field and dark-field modes cannot be used to form high-resolution images. High-resolution images are interference patterns created by phase differences of the transmitted beam after it is diffracted by the specimen. For HRTEM, a wide objective aperture is therefore needed that includes both the forward scattered electron beam and the diffracted electron beams.

A TEM also has a diffractive mode for making diffraction patterns of the specimen. In diffraction mode, the objective aperture is removed and the settings of the objective lens are modified such that its back focal plane falls onto the viewing screen. Selected area (electron) diffraction (SAED) can be used to make a diffraction pattern of a selected area of the specimen. Usually, the specimen is first checked in imaging mode, where the area of interest is selected. The inter-

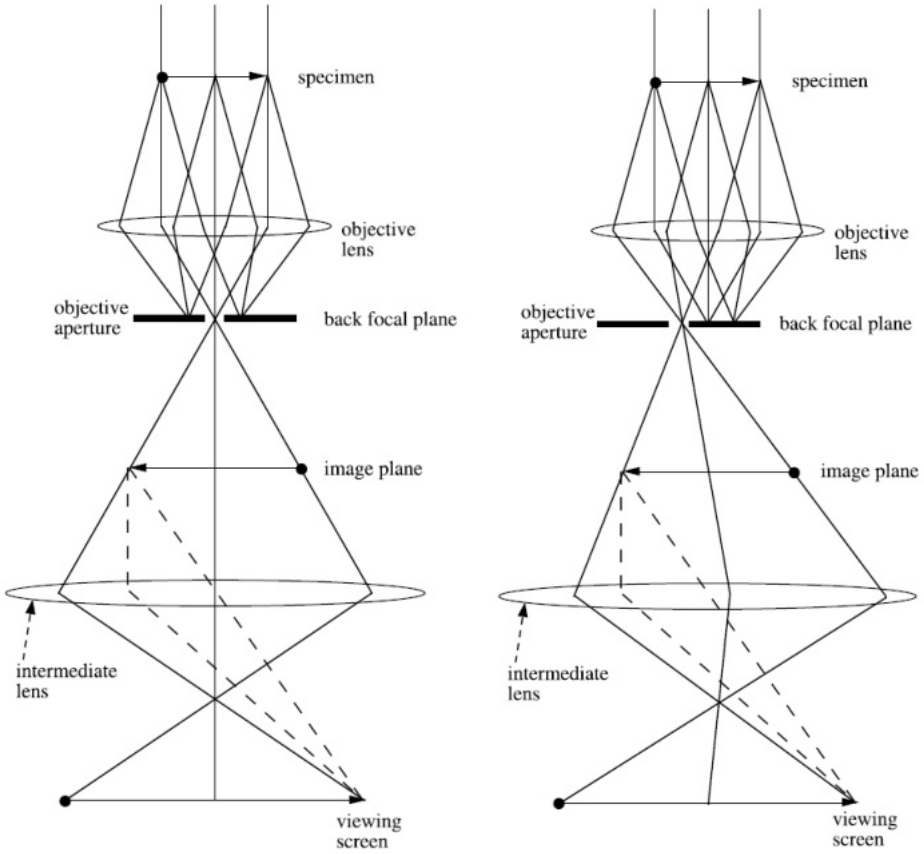

Figure 3: Left: bright-field mode. Right: dark-field mode. Reprinted from [9].

mediate aperture is then inserted around the selected area.

After passing the intermediate and projector lens, the electron beam falls onto the viewing screen where the image is recorded. This used to be a fluorescent screen for direct observation. Nowadays, usually a digital camera takes care of the imaging, which can be viewed in real time. The images can then be analysed on a computer. For TEM to be effective, the sample has to be conductive. If the sample is not conducting, electrons will accumulate in the sample and poor images will be obtained due to charging effects [9].

TEM samples are usually mounted on a copper grid. When doing in-situ TEM, the sample is deposited on a special heating chip. The heating chip that is used in this work is called *Wildfire* by DENSsolutions. This chip has a viewable area of 850 μm^2 and a 99.5% temperature homogeneity [10]. A special chip holder is used to load the sample into the microscope. Using this heating chip enables heating of the specimen while it is inside the microscope. The temperature is controlled by a separate computer that is connected to the chip holder.

2.2. Density functional theory

Density functional theory (DFT) is a modelling method that uses approximations and simplifications to find solutions to the, otherwise impossible to solve, many-body Schrödinger equation. DFT is mainly used by physicists and chemists to find the electronic structure and ground state energy of many-body systems, in particular condensed matter phases. For few-body systems, it is possible to accurately determine the wavefunctions and corresponding energies using the Schrödinger equation. However, when taking into account many bodies, the Schrödinger equation becomes much more complex. For such many-body Schrödinger equations, it is impossible to find corresponding wavefunctions because the calculations that are required to find these wavefunctions cannot be executed by our current technology. In order to still find accurate energies for these many-body systems, the fact that there is a relation between the electron density and the ground state energy can be used. This relation however, is not exactly known and therefore has to be approximated. By using these approximated density functionals, relatively easy to perform calculation can be used to compute the energies of these many-body systems.

One of the approximations is the so called Born-Oppenheimer approximation. This approximation uses the fact that the electrons move significantly faster than the nucleus of an atom. Therefore, the nucleus can be taken as stationary and the Schrödinger equation reduces to an electron only Schrödinger equation, where the nucleus is included as an external potential. The relation between the electron density and the ground state energy comes from the Hohenberg-Kohn theorems. The first Hohenberg-Kohn theorem proves that the Hamilton operator of the many-body system is uniquely determined by the electron density of the system. The next problem is how to ascertain that a certain electron density is the true ground state density of your system. This is tackled in the second Hohenberg-Kohn theorem, where the variational principle is used to prove that the true ground state density of the system delivers the lowest energy [11].

For the actual determination of these density functionals, the Kohn-Sham approach is used. Kohn and Sham realized it was not possible to accurately determine the kinetic energy through an explicit functional, so instead they tried to exactly calculate as much of the kinetic energy contributions as possible and to only use an approximation for the unsolvable remainder. A non-interacting reference system with the density of the true interacting system is used to accurately calculate a part of the kinetic energy. The energy terms resulting from the Coulomb interactions and the nuclei are added. The remainder, the exchange, correlation, and remaining part of the kinetic energy, is then included by adding an exchange-correlation potential that is a functional of the density. This exchange-correlation potential is the only unknown and has to be approximated to find the energy of the system [12].

A DFT calculation starts by approximating the exchange-correlation potential, from which the total effective potential is calculated. With this effective potential, the Kohn-Sham equations

are solved and the energy is calculated. A final consistency check is performed before the final output is given. Note that if the exchange-correlation functional is exactly known, the energy obtained by the DFT calculation is the exact energy of the system. Further improvements in DFT can therefore be made by finding better approximations for the exchange-correlation potential.

2.3. VASP

For the DFT calculations, the Vienna ab initio simulation package (VASP) version 5.4.1 is used [13, 14, 15, 16]. VASP is a plane-wave code for density functional calculations developed by Kresse and his coworkers. It computes an approximate solution to the many-body Schrödinger equation using DFT as described above. It can also approximate a solution for the many-body Schrödinger equation using the Hartree-Fock approximation, but that will not be used for this thesis. VASP is based on the projector-augmented wave (PAW) method, which is a plane-wave method that was first described by Blöchl [17]. There are generally two methods for calculating electronic structures, the plane-wave method and a method that uses orbital-type basis functions. Both methods can perform equally well on small systems. On larger systems however, the plane-wave method has a much lower computational cost compared to the method that uses orbital-type basis functions.

VASP uses efficient iterative matrix diagonalisation techniques to determine the electronic groundstate. These techniques are based on the RMM-DIIS inversion of iterative subspace and the blocked Davidson scheme. This is combined with an efficient mixing scheme, again based on the RRM-DIIS strategy. Together with a self-consistency cycle to improve the charge-density, this is what VASP uses to efficiently calculate the Kohn-Sham ground state [18].

To start a DFT calculations, several input files need to be supplied in VASP. These are the INCAR, POSCAR, KPOINTS and POTCAR files. The INCAR file defines the settings that VASP uses to perform the calculation. The POSCAR file contains the atomic positions of the cell that has to be calculated. The KPOINTS file defines the k-point grid. The POTCAR file contains the pseudopotentials for each atom in the cell. Additionally, a job file has to be supplied to submit a calculation to the computer, which contains the jobname and the number of cores that will be used for the calculation.

After a VASP calculation is finished, three major output files can be found. These are the OUTCAR, OSZICAR and CONTCAR files. The OUTCAR is the most important output file in VASP. It first gives a summary of the supplied input files and detailed job information, after which it gives information about the ionic steps, eigenvalues, energies, forces on the atoms, stress-tensors, charges, magnetism and dielectric properties. The OSZICAR is a short version of the OUTCAR that only contains information about the ionic steps and corresponding energies.

The CONTCAR contains atomic positions after optimization and has the same format as the POSCAR.

3. Methods

3.1. Imaging

The TEM images were obtained by Xiaodan Chen, Msc, on a FEI Talos F200X. The MoO_3 nanoparticles were purchased from Sigma-Aldrich and had a size of approximately 200 nm - 1 μm. The MoO_3 nanoparticle solution was dropcasted on the DENSsolutions *Wildfire* heating chip. The nanoparticles were first heated from 20 °C to 600 °C with 100 °C steps. In a later experiment, the nanoparticles were first heated from 20 °C to 400 °C with 100 °C steps, followed by 25 °C steps until a temperature of 700 °C was reached.

3.2. Determining DFT settings

In order to find accurate results that require the least computational power, the optimal energy cut-off and k-mesh settings have to be determined. The cut-off energy was sampled from 300 to 900 eV, while the k-points were kept at 20x6x20 along the reciprocal lattice parameters, and the energy per atom was determined. The same was done for the k-points, where values between 2x1x2 and 26x8x28 were sampled while the cut-off energy was kept at 750 eV. From these calculations, the best settings were determined to be 800 eV for the energy cut-off and 6x2x6 for the k-points (see appendix A). These optimizations were only determined for MoO_3. Since MoO_2 has a similar composition, we can assume the optimal cut-off energy is the same as that of MoO_3. The k-points for MoO_2 were rescaled with respect to those of MoO_3, resulting in a k-mesh of 6x8x6.

3.3. Testing DFT functionals

Three different functionals were tested to find which one gives the best agreement with experimental values. These are the standard GGA-PBE [19, 20] functional which is a version of the general gradient approximation (GGA), the DFT-D3 [21] functional which adds a van der Waals interaction to the GGA-PBE functional, and the optB88-vdW [22, 23, 24, 25], which is a non-local exchange-correlation functional that accounts for dispersion interactions and is optimized for the correlation part. For each functional, the cell was relaxed with the optimal energy cut-off and k-mesh settings. The lattice parameters were compared to experimental values [26, 27, 28], see table 1.

Table 1: Lattice parameters for MoO_3, Mo_4O_{11}, and MoO_2 for different functionals compared to experimental values. The deviation from the experimental value is given in percentages.

	Functional	a (Å)	Δa (%)	b (Å)	Δb (%)	c (Å)	Δc (%)
MoO_3	Experimental	3.962		13.856		3.698	
	GGA-PBE	3.94	0.58	15.85	14.42	3.69	0.28
	DFT-D3	3.93	0.87	14.35	3.59	3.69	0.31
	optB88-vdW	3.91	1.25	14.07	1.57	3.71	1.09
Mo_4O_{11}	Experimental	24.29		5.457		6.752	
	GGA-PBE	24.73	1.83	5.52	1.16	6.81	0.89
	DFT-D3	24.71	1.72	5.52	1.16	6.80	0.74
	optB88-vdW	24.66	1.52	5.49	0.65	6.78	0.42
MoO_2	Experimental	5.608		4.842		5.517	
	GGA-PBE	5.39	3.93	4.90	1.15	5.50	0.37
	DFT-D3	5.37	4.28	4.88	0.84	5.48	0.71
	optB88-vdW	5.40	3.75	4.89	1.07	5.48	0.61

For MoO_3, the GGA-PBE functional performs poorly in the b-direction. The DFT-D3 and optB88-vdW functionals are great improvements compared to the GGA-PBE functional. The optB88-vdW functional has the best parameters compared with the experimental values. For MoO_2 and Mo_4O_{11}, the best functional is again optB88-vdW, although this time the other functionals perform almost equally well. Since it is known that the optB88-vdW functional performs poorly in vacuum, the DFT-D3 functional will be used for all further density functional calculations.

3.4. Energy calculations

The energies of the different molybdenum structures were calculated by simply relaxing the experimental unit cell, both the lattice parameters and atomic coordinates, for the settings and functionals given above. The energy of the relaxed structure can then be found in the OSZICAR output file. The energy of an O_2 molecule was also calculated, to compare the energies of the MoO_3, Mo_4O_{11}, and MoO_2 structures. For the O_2 molecule, the DFT-D3 functional was used in combination with a k-mesh of 1x1x1 and a cut-off energy of 900 eV. Also magnetism was taken into account. The surface energy of the (010) surface of MoO_3 was calculated by making a MoO_3 supercell consisting of 5 stacked unit cells of MoO_3 with 4 unit cells of vacuum on top, see figure 11. This supercell was relaxed using the same settings as the unitcell, but with the k-points scaled accordingly. The surface energy is then given by:

$$(MoO_3)_{(010)} = \frac{E(supercell) - 5E(unitcell)}{2A} \tag{1}$$

where A is the area of the surface.

Using the relaxed supercell, the energy it takes to exfoliate one layer of MoO_3 was calculated by shifting the upper layer upwards in 10 steps of 0.02 in direct coordinates. A possible interface between the MoO_3 and MoO_2 structures was investigated by transforming the MoO_2 to fit MoO_3. For the visualisation of the structures, which was also used in some figures, VESTA was used [29].

4. Results

4.1. Nanoparticles heating

The nanoparticles were heated from room temperature to 700 °C. Figure 4 shows the MoO_3 at different temperatures. It can be seen that up to 500 °C, the particles did not change significantly. Starting from 550 °C, the particles started to disintegrate. This disintegration continued at 600 °C and 700 °C until the whole nanoparticle had broken up in small flakes.

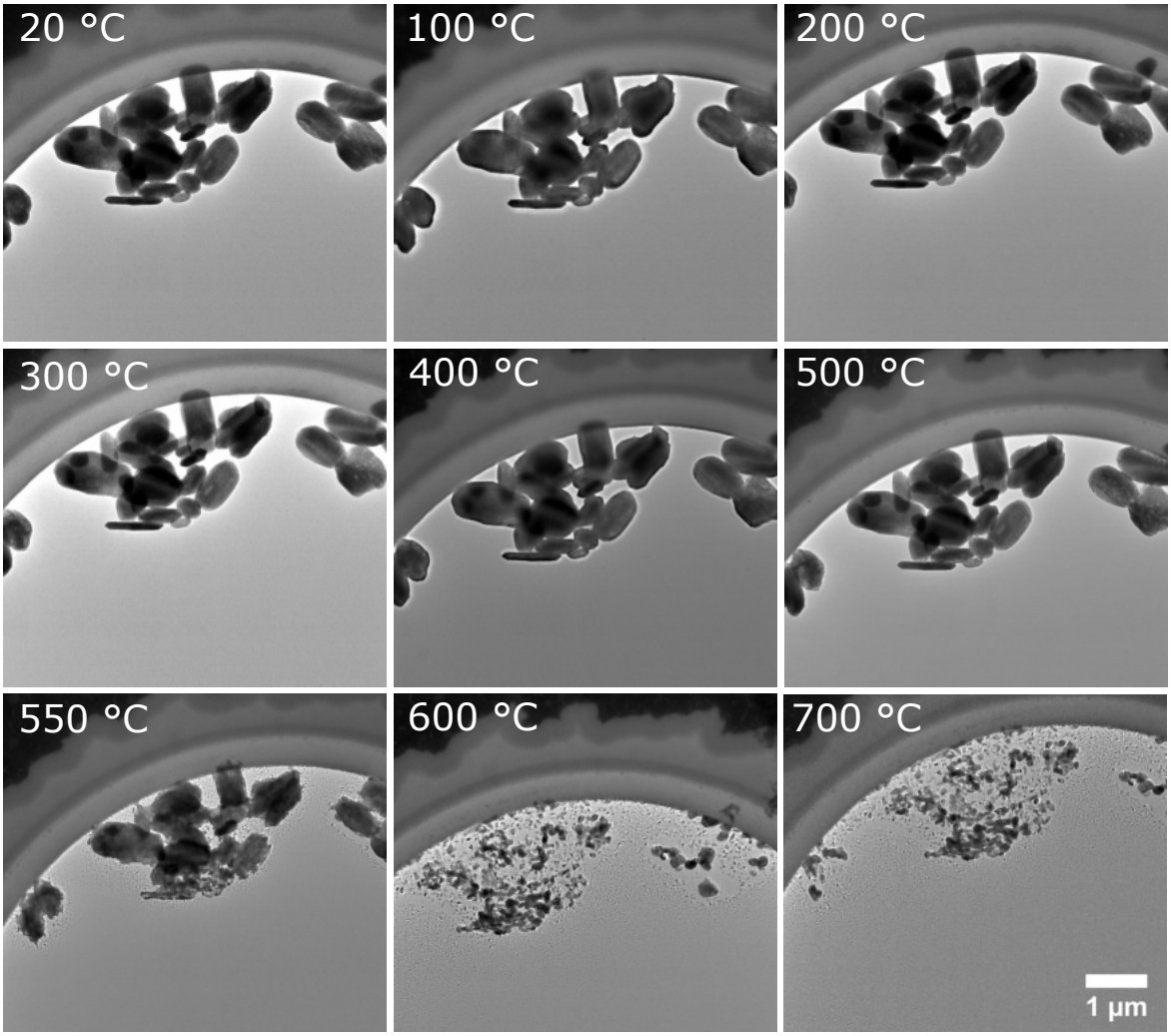

Figure 4: TEM images of the nanoparticles from 20 °C to 700 °C.

A selected area diffraction (SAED) pattern of the flakes was recorded at 600 °C, see figure 5. The diffraction pattern shows that the flakes are monoclinic MoO_2. The MoO_3 nanoparticles are therefore reduced to MoO_2 after heating to 600°C.

Several HRTEM images were taken as well. In figure 6, some of these images are displayed with the corresponding FFT patterns. These images show that monoclinic MoO_2 is formed starting from 500 °C. Furthermore, orthorhombic Mo_4O_{11} was found at 500 °C and 550 °C, but

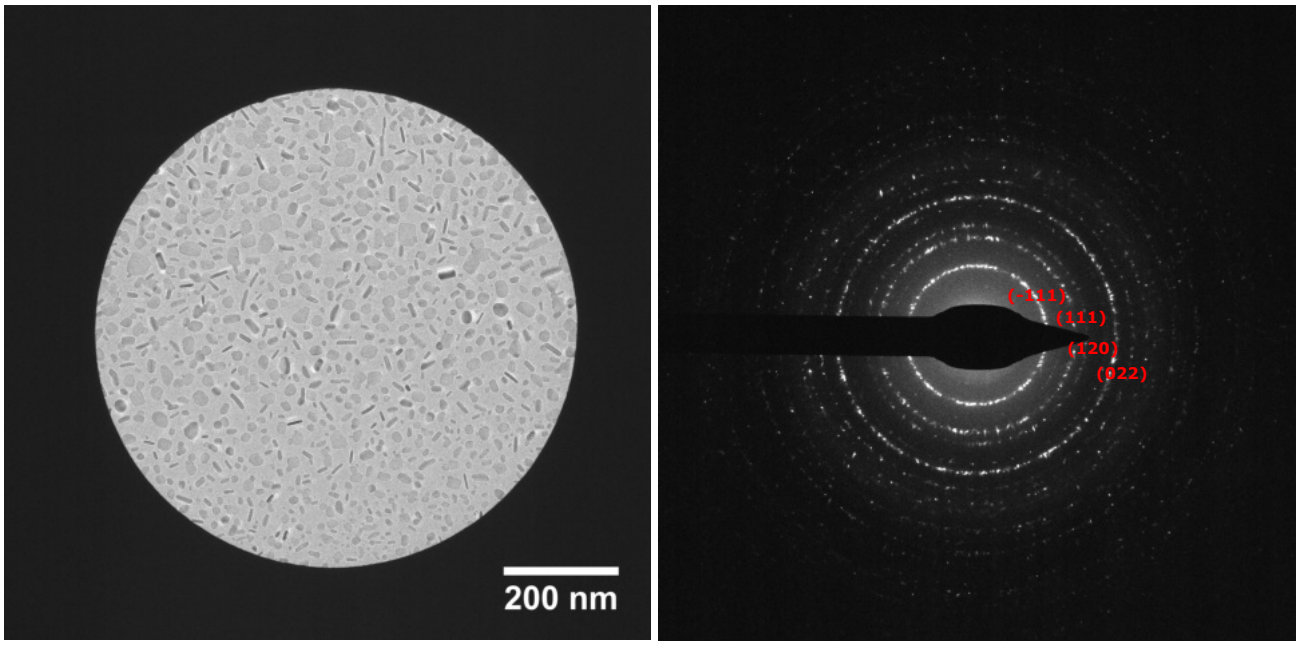

Figure 5: SAD of the flakes at 600 °C. Left: Selected area for the diffraction. Right: Indexed diffraction pattern of the selected area, confirming the monoclinic MoO_2 structure.

disappeared at 625 °C.

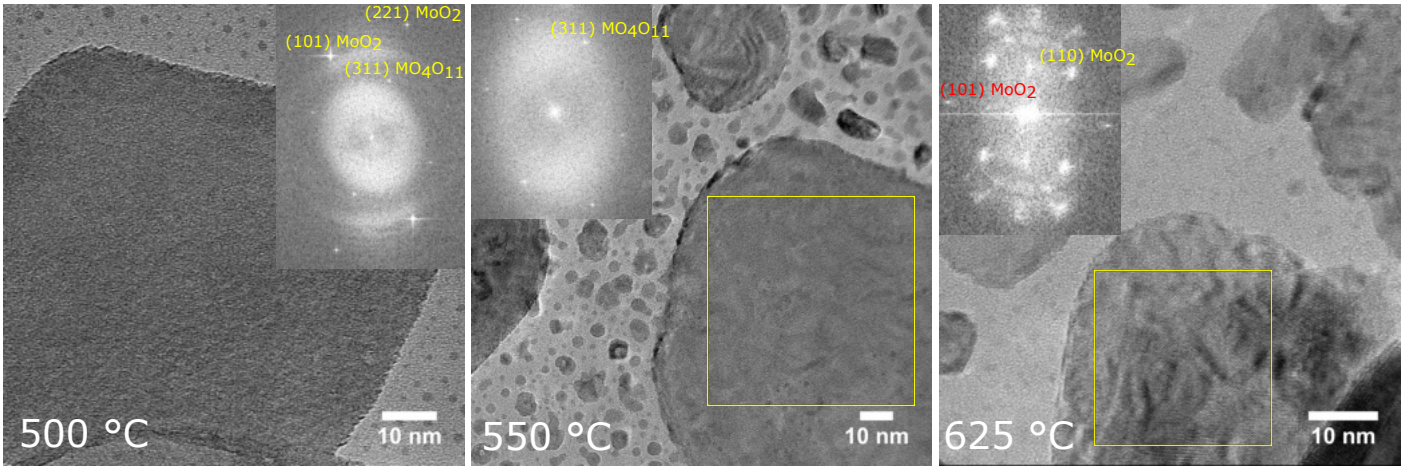

Figure 6: HRTEM images of the flakes with FFT showing monoclinic MoO_2 and orthorhombic Mo_4O_{11}.

A diffraction pattern was also taken at 500 °C, see figure 7. The diffraction pattern corresponds to the MoO_3 structure. Several diffraction spots were split as indicated by the circles in figure 7. These split spots are caused by MoO_3 layers that have a small mistilt with respect to each other. This indicates that the MoO_3 layers were exfoliated partly during the heating. The exfoliation of MoO_3 has been further examined with DFT.

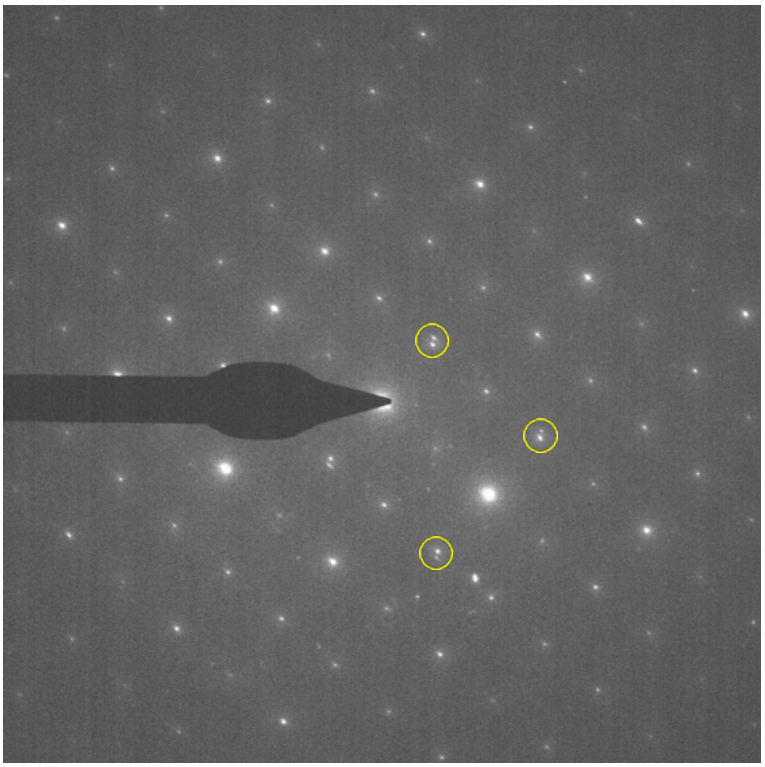

Figure 7: Diffraction pattern taken at 500 °C, corresponding to the MoO_3 structure. The encircled splitted spots indicate MoO_3 layers that are partly exfoliated.

4.2. DFT calculations

The MoO_3, Mo_4O_{11}, and MoO_2 structures were first relaxed using the DFT-D3 functional, as was described in the methods section. The energy of the relaxed MoO_3 is -8.55 eV/atom, the energy of the relaxed Mo_4O_{11} is -8.71 eV/atom, and the energy of the relaxed MoO_2 unitcell is -9.10 eV/atom. The calculated energy of the O_2 molecule is -4.94 eV/atom. The optimized O_2 bondlength is 1.23 Å, which corresponds to the reference value of 1.21 Å[30].

The reduction reaction of MoO_3 to MoO_2 is given by:

$$MoO_3 \rightarrow MoO_2 + \frac{1}{2}O_2 \tag{2}$$

meaning that for every MoO_3 unit that is reduced to MoO_2, 1.97 eV (0.49 eV/atom) has to paid. In a similar way, the reduction reaction of MoO_3 to Mo_4O_{11} is given by:

$$4MoO_3 \rightarrow Mo_4O_{11} + \frac{1}{2}O_2 \tag{3}$$

meaning that for every MoO_3 unit that is reduced to Mo_4O_{11}, 0.31 eV (0.08 eV/atom) has to be paid. Since energy has to be paid in order to reduce MoO_3, the reduction of MoO_3 is not energetically favourable at 0 K. Because the energy cost to form Mo_4O_{11} is lower than the cost to form MoO_2, it is expected that Mo_4O_{11} will form before MoO_2. It is also possible to form Mo_4O_{11} in a reaction between MoO_3 and the already formed MoO_2:

$$3MoO_3 + MoO_2 \rightarrow Mo_4O_{11} \tag{4}$$

which actually results in an energy gain of 0.74 eV per formed unit of Mo_4O_{11} (0.05 eV/atom).

The MoO_3 supercell was also relaxed, using the same settings and functional as for the MoO_3 unitcell. This resulted in an energy of -8.549 eV/atom. From this, the surface energy of the (010) MoO_3 surface was calculated using equation 1. The surface area of the (010) surface is 14.459 $Å^2$, which was calculated from the lattice parameters of the relaxed MoO_3 supercell. The resulting surface energy is $1.17 \cdot 10^{-2}$ eV/$Å^2$, which is 0.187 J/m^2.

It was seen that the MoO_3 layers exfoliated partly during heating in the TEM. This was investigated by calculating the exfoliation energy of MoO_3, which was done by manually shifting the upper layer of the MoO_3 supercell upwards, see figure 11, and calculating the energy of the supercell at each step. Figure 8 shows the energy path of the manual exfoliation, where the energy changed from -8.55 eV/atom to -8.54 eV/atom. The energy cost to remove one layer from the MoO_3 bulk is therefore 0.36 eV for one layer of the supercell (per Mo_2O_6 unit). The surface that is created when exfoliating one layer of MoO_3 is two times a [010] surface. The energy that has to be paid to create this surface is therefore 0.34 eV, which is almost equal to the total energy cost. The energy path shows that the activation energy is equal to the total energy change. This indicates that the MoO_3 layers are weakly bound.

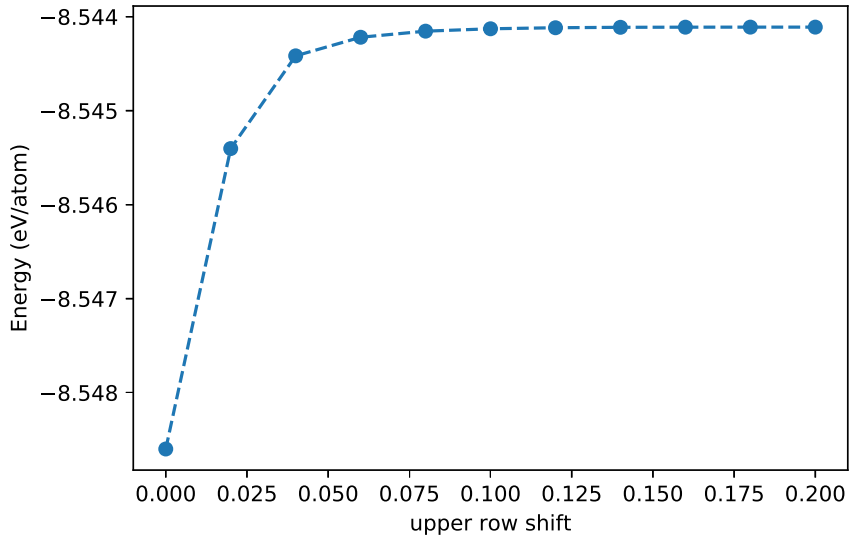

Figure 8: Exfoliation energy of MoO_3 calculated by manually shifting the upper layer upwards.

It was investigated if an interface between MoO_3 and MoO_2 could exist. After relaxation of the MoO_2 unitcell, the cell had an angle, as can bee seen in figure 9. In order to fit this cell on a MoO_3 cell, the angle has to be removed. This was done by modifying the c-axis to be perpendicular to **a** and **b** according to: c*=2**c**-**a**. After this transformation, it was clear that the

square pattern had an angle of 45 °. In order to match the square pattern of MoO_3, this angle was removed by doubling the b-axis and redefining the lattice parameters by a 45 ° rotation around the a-axis. The result of the transformations can be seen in figure 10.

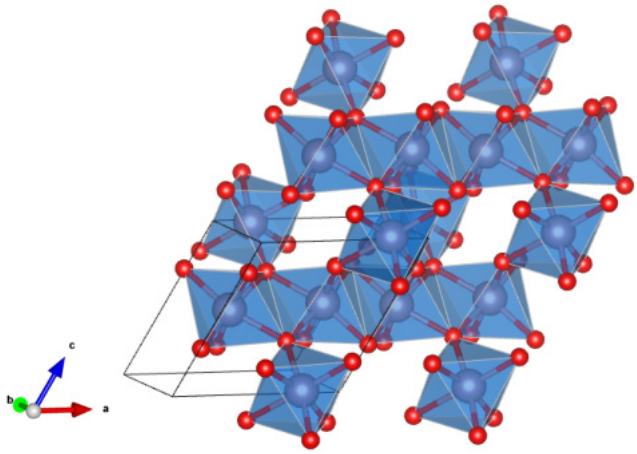

Figure 9: MoO_2 unitcell after relaxation.

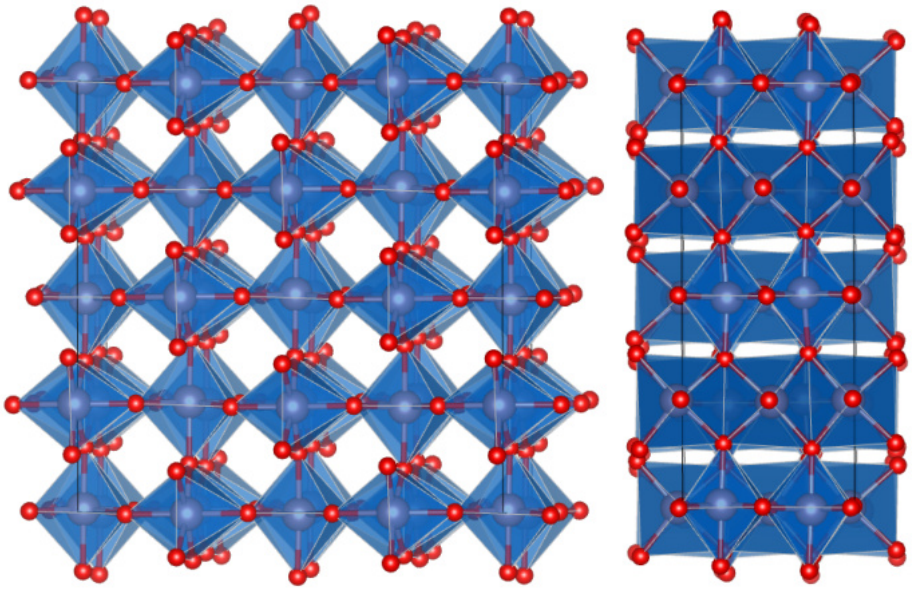

Figure 10: (100) (left) and (010) (right) surface of the transformed MoO_2 structure.

The structure of MoO_2 shown in figure 10 is now similar to the MoO_3 structure shown in figure 1. However, in order to make an interface between the two structures, a lattice mismatch of around 30% exists in one direction, see table 2. Therefore, when the surface of MoO_3 reduces to MoO_2, the lattice mismatch between the two structures likely causes the MoO_2 to chip off.

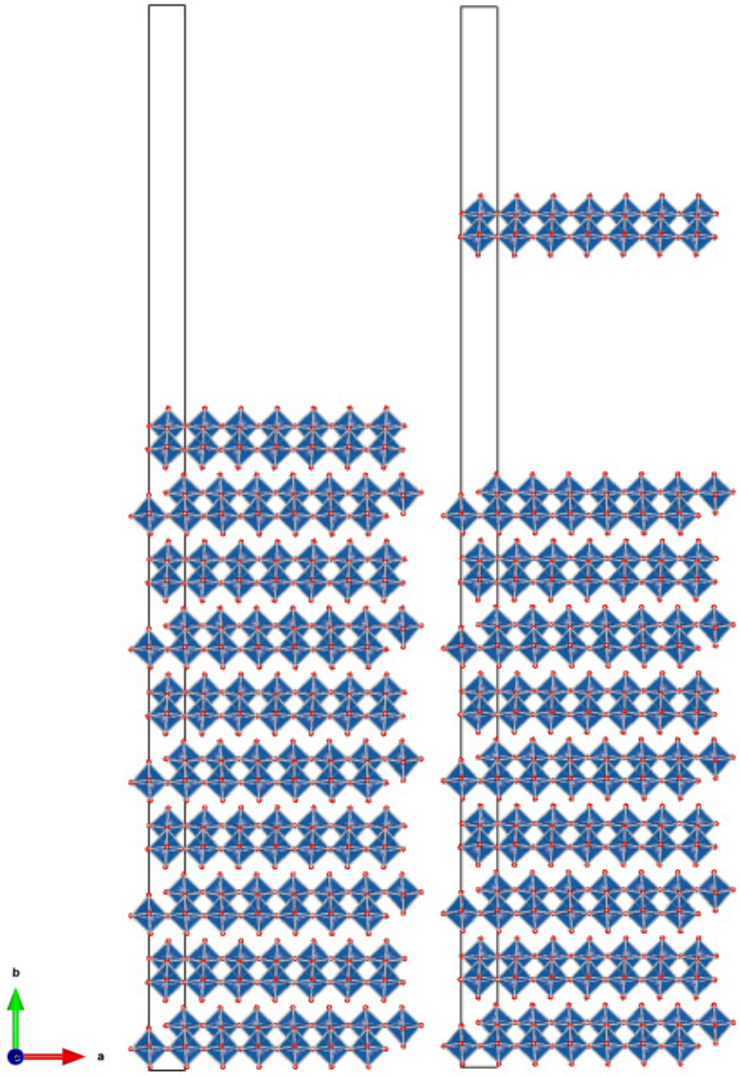

Figure 11: The MoO_3 supercell without shifted top layer (left) and with the highest calculated upwards shift (right).

Table 2: Lattice constants of the transformed MoO_2 unitcell and the MoO_3 unitcell, from which the interface has to be formed.

	transformed MoO_2 (Å)	MoO_3 (Å)
a	5.61	3.93
b	13.9	14.4
c	13.9	3.69

5. Discussion

The DFT calculations indicate that the reduction of MoO_3 is not energetically favourable at 0 K. However, the reaction does take place at elevated temperatures in the vacuum of the TEM. This is because the heating of the sample increases the thermal vibrations, causing the chemical bonds to break. The vacuum then removes any oxygen that escapes from the structure, causing the chemical reaction equilibrium to shift towards reduction.

From the DFT calculations, it cannot be proven whether the found Mo_4O_{11} is formed as an intermediate, or in a side reaction. There was little evidence of Mo_4O_{11} and only at 500 and 550 °C. It could therefore be possible for the Mo_4O_{11} to act as an intermediate that quickly reduces further to MoO_2. Another possibility is that the Mo_4O_{11} is formed in a side reaction, after which it also reduces to MoO_2 at higher temperatures. Because the side reaction is energetically favourable at 0 K, it is more likely that the Mo_4O_{11} will form in the side reaction.

For the calculation of the exfoliation energy of MoO_3, the upper layer of the supercell was manually shifted upwards. Initially, a method which uses selective dynamics was chosen for the calculation of the exfoliation energy. Selective dynamics is a VASP feature that can be turned on by modifying the POSCAR. When using selective dynamics, it can be specified which atoms in the supercell can move and which atoms are fixed. The upper Mo atom can then be shifted upwards and fixed. When relaxed, the other atoms will move towards this shifted Mo atom. The selective dynamics would have given a more accurate description of the exfoliation of a layer of MoO_3. However, the selective dynamics calculations gave errors that could not be bypassed. It was therefore chosen to manually shift the entire upper layer of the MoO_3 supercell.

6. Conclusion

MoO_3 nanoparticles were heated with in-situ TEM. The MoO_3 nanoparticles disintegrated starting from 550 °C. A selected area diffraction showed that the disintegrated nanoparticles flakes had the monoclinic MoO_2 crystal structure. Several high resolution TEM images showed that MoO_2 was present starting from 500 °C. Also orthorhombic Mo_4O_{11} was found at 500 °C and 550 °C, but was not seen at temperatures above 600 °C. A different diffraction pattern taken at 500 °C showed the onset of exfoliation of MoO_3 by the presence of splitted diffraction spots. DFT was used to investigate these findings.

From the DFT calculations, it was found that it costs energy to reduce MoO_3 at 0 K. The energy cost to reduce MoO_3 to Mo_4O_{11} is lower than the cost to reduce MoO_3 to MoO_2. It was also found that the formation of Mo_4O_{11} from a reaction between MoO_3 and MoO_2 is favourable at 0 K. It is therefore likely that Mo_4O_{11} is formed in this side reaction. The reduction of MoO_3 costs energy at 0 K. It is therefore not a favourable reaction at this temperature. Perhaps the increase in temperature and the vacuum of the TEM cause the reaction to become favourable at higher temperature.

The surface energy of a MoO_3 (010) surface was calculated to be 0.187 J/m^2. The exfoliation energy of MoO_3 was calculated to be 0.36 eV for one layer of the supercell. This is a little higher than the energy it takes to create the surfaces resulting from the exfoliation, which is 0.34 eV. The exfolation energy path showed that the activation energy of the exfoliation is equal to the total energy change, meaning that the layers in MoO_3 are weakly bound.

The interface between the MoO_3 and MoO_2 structures was investigated and was found to probably not exist. The large lattice mismatch that is present within this interface probably causes the MoO_2 layer to chip as soon as it is created, causing the MoO_3 nanoparticle to eventually disintegrate.

Further research is needed to prove if Mo_4O_{11} is an intermediate or formed in a side reaction, or perhaps both. Also, assessing the stability of more of the substoichiometric phases of molybdenum oxide would be useful, to explain why only Mo_4O_{11} is found in the reduction of MoO_3 to MoO_2.

References

[1] Lahrs Kihlborg. "Studies on molybdenum oxides". In: *Acta Chem. Scand* 13.954 (1959), e962.

[2] Arumugam Manivel et al. "Synthesis of MoO3 nanoparticles for azo dye degradation by catalytic ozonation". In: *Materials Research Bulletin* 62 (2015), pp. 184–191.

[3] MB Sreedhara et al. "Synthesis, characterization, and properties of few-layer MoO3". In: *Chemistry–An Asian Journal* 8.10 (2013), pp. 2430–2435.

[4] Jerzy Haber and Erwin Lalik. "Catalytic properties of MoO3 revisited". In: *Catalysis today* 33.1-3 (1997), pp. 119–137.

[5] Robert Karl Grasselli. "Fundamental principles of selective heterogeneous oxidation catalysis". In: *Topics in Catalysis* 21.1-3 (2002), pp. 79–88.

[6] Robert Burch. "Preparation of high surface area reduced molybdenum oxide catalysts." In: *Journal of the Chemical Society, Faraday Transactions 1: Physical Chemistry in Condensed Phases* 74 (1978), pp. 2982–2990.

[7] Thorsten Ressler et al. "In situ XAS and XRD studies on the formation of Mo suboxides during reduction of MoO3". In: *The Journal of Physical Chemistry B* 104.27 (2000), pp. 6360–6370.

[8] PA Spevack and NS McIntyre. "Thermal reduction of molybdenum trioxide". In: *The Journal of Physical Chemistry* 96.22 (1992), pp. 9029–9035.

[9] Brent Fultz and James M Howe. *Transmission Electron Microscopy and Diffractometry of Materials*. 4th ed. Springer-Verlag Berlin Heidelberg, 2013. Chap. 2, pp. 59–109. ISBN: 9783642297618.

[10] DENSsolutions. *The revolutionary Wildfire Nano-Chip*. DENSsolutions. URL: `https://denssolutions.com/products/wildfire/nano-chip/`.

[11] Wolfram Koch and Max C Holthausen. *A Chemist's Guide to Density Functional Theory*. 2nd ed. John Wiley & Sons, 2008. Chap. 4, pp. 33–37. ISBN: 9783527303724.

[12] Wolfram Koch and Max C Holthausen. *A Chemist's Guide to Density Functional Theory*. 2nd ed. John Wiley & Sons, 2008. Chap. 5, pp. 41–46. ISBN: 9783527303724.

[13] Georg Kresse and Jürgen Hafner. "Ab initio molecular dynamics for liquid metals". In: *Physical Review B* 47.1 (1993), p. 558.

[14] Georg Kresse and Jürgen Hafner. "Ab initio molecular-dynamics simulation of the liquid-metal–amorphous-semiconductor transition in germanium". In: *Physical Review B* 49.20 (1994), p. 14251.

[15] Georg Kresse and Jürgen Furthmüller. "Efficiency of ab-initio total energy calculations for metals and semiconductors using a plane-wave basis set". In: *Computational materials science* 6.1 (1996), pp. 15–50.

[16] Georg Kresse and Jürgen Furthmüller. "Efficient iterative schemes for ab initio total-energy calculations using a plane-wave basis set". In: *Physical review B* 54.16 (1996), p. 11169.

[17] Peter E Blöchl. "Projector augmented-wave method". In: *Physical review B* 50.24 (1994), p. 17953.

[18] Jürgen Hafner. "Ab-initio simulations of materials using VASP: Density-functional theory and beyond". In: *Journal of computational chemistry* 29.13 (2008), pp. 2044–2078.

[19] John P Perdew, Kieron Burke, and Matthias Ernzerhof. "Generalized gradient approximation made simple". In: *Physical review letters* 77 (1996), p. 3865.

[20] John P Perdew, Kieron Burke, and Matthias Ernzerhof. "Erratum: Generalized gradient approximation made simple". In: *Physical review letters* 78 (1997), p. 1396.

[21] Stefan Grimme et al. "A consistent and accurate ab initio parametrization of density functional dispersion correction (DFT-D) for the 94 elements H-Pu". In: *The Journal of chemical physics* 132.15 (2010), p. 154104.

[22] Guillermo Román-Pérez and José M Soler. "Efficient implementation of a van der Waals density functional: application to double-wall carbon nanotubes". In: *Physical review letters* 103.9 (2009), p. 096102.

[23] Max Dion et al. "Van der Waals density functional for general geometries". In: *Physical review letters* 92.24 (2004), p. 246401.

[24] Jiří Klimeš, David R Bowler, and Angelos Michaelides. "Chemical accuracy for the van der Waals density functional". In: *Journal of Physics: Condensed Matter* 22.2 (2009), p. 022201.

[25] Jiří Klimeš, David R Bowler, and Angelos Michaelides. "Van der Waals density functionals applied to solids". In: *Physical Review B* 83.19 (2011), p. 195131.

[26] Husin Sitepu, Brian H O'Connor, and Deyu Li. "Comparative evaluation of the March and generalized spherical harmonic preferred orientation models using X-ray diffraction data for molybdite and calcite powders". In: *Journal of Applied Crystallography* 38.1 (2005), pp. 158–167.

[27] Arne Magneli and Georg Andersson. "On the MoO2 structure type". In: *Acta Chem. Scand* 9.1 (1955), pp. 1378–1381.

[28] S Åsbrink and L Kihlborg. "A study of the crystal symmetry and structure of orthorhombic Mo4O11 by least-squares techniques". In: *Acta Chem. Scand* 18.6 (1964), pp. 1571–1573.

[29] Koichi Momma and Fujio Izumi. "VESTA 3 for three-dimensional visualization of crystal, volumetric and morphology data". In: *Journal of applied crystallography* 44.6 (2011), pp. 1272–1276.

[30] Leslie Ernest Sutton. *Tables of Interatomic Distances and Configuration in Molecules and Ions: Supplement 1956-59*. 18. Chemical Society, 1965.

A. Cut-off and k-points settings

It is important to find proper settings for the cut-off energy and k-points before starting the actual calculations. This ensures that the calculations take the least computational power but still produce accurate results. Figure 12 and 13 show the energy differences calculated for different cut-off energy and k-points settings. The cut-off energy and k-points were considered sufficiently high when the difference compared to the highest setting was no more than ± 0.5 meV/atom. For the cut-off energy, this criterion was reached starting from 750 eV. Because 800 eV was a high improvement compared to 750 eV, 800 eV was chosen as the cut-off energy setting for further calculations. For the k-points, the criterion was reached starting from 4x1x4. However, 6x2x6 was a great improvement compared to 4x1x4. Therefore 6x2x6 was chosen as the k-points value for further calculations. All calculations were performed with the GGA-PBE functional [19, 20]. Table 3 contains the energies and energy differences for all calculated values of the cut-off energy and k-mesh.

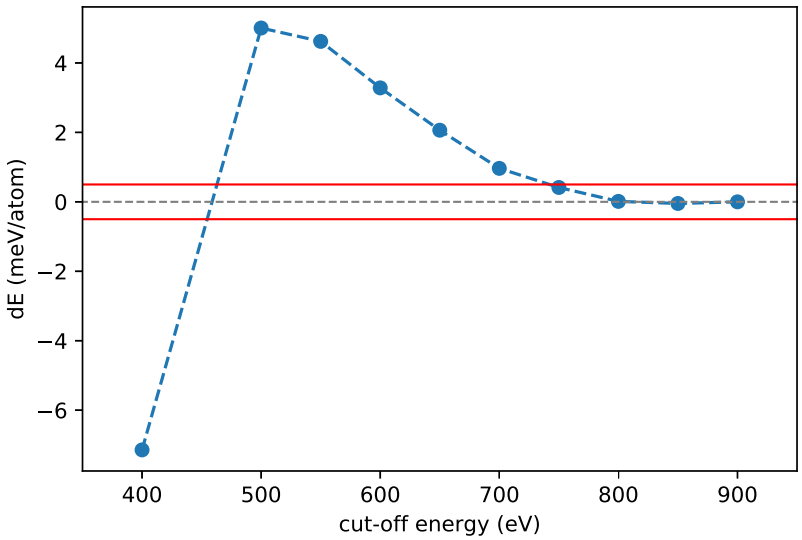

Figure 12: Calculated energy differences per atom of MoO_3 for different cut-off energies compared to the highest setting (900 eV). The red lines indicate a difference of ± 0.5 meV/atom. All cut-off energies were determined while the k-points were kept at 20x6x20. The energy difference for a cut-off energy for 300 eV was left out because it is much higher than the rest of the results, see table 3.

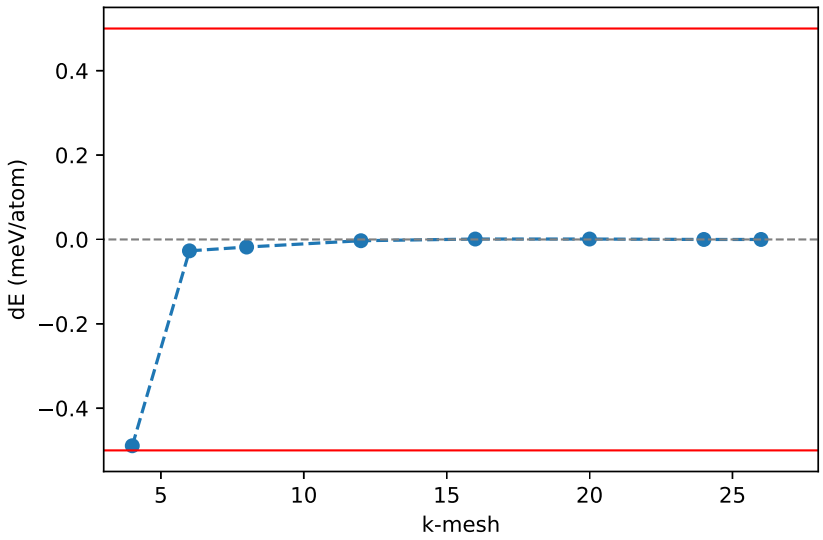

Figure 13: Calculated energy differences per atom of MoO_3 for different k-points values compared to the highest setting (26x8x28). The red lines indicate a difference of ± 0.5 meV/atom. All kmesh energies were determined while the cut-off energy was kept at 750 eV. The values on the x-axis represent the first k-point value. The energy difference for a k-mesh of 2x1x2 was left out because it is much higher than the rest of the results, see table 3.

Table 3: Calculated energies per atom and difference with respect to the highest setting for different cut-off energies (a) and k-mesh settings (b) of the MoO_3 unitcell.

(a)

cut-off energy (eV)	E (eV/atom)	dE (meV/atom)
300	−8.446	−97.104
400	−8.356	−7.144
500	−8.344	5.006
550	−8.344	4.621
600	−8.346	3.282
650	−8.347	2.063
700	−8.348	0.964
750	−8.349	0.414
800	−8.349	0.013
850	−8.349	−0.047
900	−8.349	0.000

(b)

k-points	E (eV/atom)	dE (meV/atom)
2x1x2	−8.301	47.159
4x1x4	−8.349	−0.489
6x2x6	−8.348	−0.027
8x4x8	−8.348	−0.018
12x4x12	−8.348	−0.003
16x6x16	−8.348	0.001
20x6x20	−8.348	0.001
24x8x24	−8.348	0.000
26x8x28	−8.348	0.000